

# IB-U-Nets: Improving medical image segmentation tasks with 3D Inductive Biased kernels

Shrajan Bhandary<sup>1</sup>, Zahra Babaiee<sup>1</sup>, Dejan Kostyszyn<sup>2,3,4</sup>, Tobias Fechter<sup>2,3,4</sup>, Constantinos Zamboglou<sup>2,3,4,5</sup>, Anca-Ligia Grosu<sup>2,3,4</sup>, Radu Grosu<sup>1</sup>

<sup>1</sup> Technische Universität Wien, Vienna, Austria

<sup>2</sup> Division of Medical Physics, Department of Radiation Oncology, Medical Center University of Freiburg, Germany

<sup>3</sup> Faculty of Medicine, University of Freiburg, Germany

<sup>4</sup> German Cancer Consortium (DKTK), Partner Site Freiburg, Germany

<sup>5</sup> German Oncology Center, European University, Limassol, Cyprus

shrajan.bhandary@tuwien.ac.at, zahra.babaiee@tuwien.ac.at, dejan.kostyszyn@uniklinik-freiburg.de, tobias.fechter@uniklinik-freiburg.de, constantinos.zamboglou@uniklinik-freiburg.de, anca.grosu@uniklinik-freiburg.de, radu.grosu@tuwien.ac.at

## Abstract

Despite the success of convolutional neural networks for 3D medical-image segmentation, the architectures currently used are still not robust enough to the protocols of different scanners, and the variety of image properties they produce. Moreover, access to large-scale datasets with annotated regions of interest is scarce, and obtaining good results is thus difficult. To overcome these challenges, we introduce IB-U-Nets, a novel architecture with inductive bias, inspired by the visual processing in vertebrates. With the 3D U-Net as the base, we add two 3D residual components to the second encoder blocks. They provide an inductive bias, helping U-Nets to segment anatomical structures from 3D images with increased robustness and accuracy. We compared IB-U-Nets with state-of-the-art 3D U-Nets on multiple modalities and organs, such as the prostate and spleen, using the same training and testing pipeline, including data processing, augmentation and cross-validation. Our results demonstrate the superior robustness and accuracy of IB-U-Nets, especially on small datasets, as is typically the case in medical-image analysis. IB-U-Nets source code and models are publicly available.

## Introduction

Manual segmentation of organs from medical images is an essential tool for diagnosis, treatment, and progression monitoring of several diseases (Goldenberg, Nir, and Salcudean 2019; Spohn et al. 2021; Singh et al. 2020; Antonelli et al. 2022; Isensee et al. 2021). Unfortunately, manual segmentation is time-consuming and underlies significant interobserver heterogeneity (Rischke et al. 2013; Steenbergen et al. 2015). Fortunately, recent advances in deep learning (DL) hold a great promise for automatic segmentation. Since the success of AlexNet (Krizhevsky, Sutskever, and Hinton 2012), the biomedical-imaging community has been investigating various convolutional neural-network architectures (CNN) to enhance cancer-detection efficiency (Singh et al. 2020). In particular, U-Nets yielded most accurate segmentation on medical datasets (Ronneberger, Fischer, and Brox

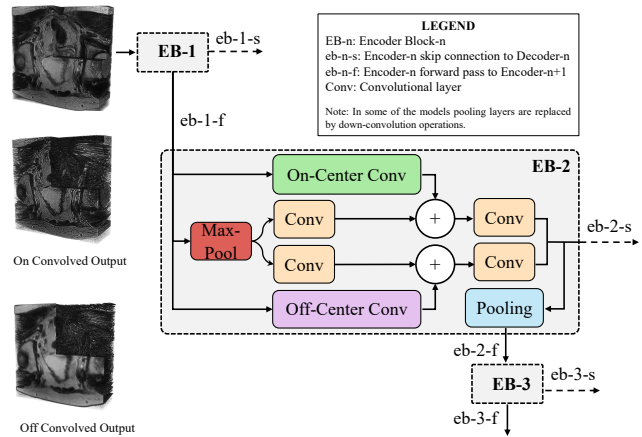


Figure 1: Extending U-Net variants with two 3D inductive biases, On and Off center-surround convolution respectively, enhances their segmentation accuracy and robustness to distribution shifts.

2015), first in 2D and later on in 3D medical-imaging scenarios (Çiçek et al. 2016). However, the U-Nets currently in use are still not sufficiently robust to images obtained from different scanners, to shape variability, and to poor tissue contrast of some organs (Gillespie et al. 2020). Moreover, the segmentation accuracy of U-Nets still leaves room for improvement, especially in small-sized 3D datasets (Litjens et al. 2017; Isensee et al. 2021).

In this paper we address the above limitations, by enhancing state-of-the-art (SOTA) 3D U-Nets, with an inductive bias (IB) inspired by the retinal-processing pathways of vertebrates. In particular, we add two 3D residual components (an on- and an off-center-surround convolution, with predefined weights) to the second encoder blocks of U-Nets (in parallel to the max-pooling component), as depicted in Figure 1. The IB provided by these components, helps the U-Nets to scrutinize and delineate anatomical structures of 3D images with increased precision, as shown in Figure 2.

For a comprehensive analysis, we implemented several

alternative architectures with IB extensions and evaluated robustness against changes in parameter values. To demonstrate the general applicability of our method we performed experiments on 3D medical multi modal image datasets containing unique organs. A limiting factor in multiple clinical studies is the low number of datasets available for training. To address this issue, we conducted multiple experiments with varying number of training datasets to test clinical suitability. We performed our experiments on two prostate-contour-annotated datasets: PROMISE-12 and MSD-prostate. PROMISE-12 (prostate MRI segmentation 2012) challenge (Litjens et al. 2014) and MSD-prostate (medical segmentation decathlon) (Simpson et al. 2019; Antonelli et al. 2021, 2022) are two of the most widely used and publicly available datasets. Additionally, we carried out experiments with the spleen dataset from medical segmentation decathlon (MSD-spleen) (Simpson et al. 2019; Antonelli et al. 2021, 2022). We created a framework, similar to the design principles of other popular frameworks such as MONAI (Consortium 2020) and nnU-Net (Isensee et al. 2021), to objectively compare and evaluate different U-Net variants. We also extended the U-Net architecture of the nnU-Net with the IB kernels to examine their effectiveness on a strong and versatile medical segmentation baseline. In particular, we provide our results for U-Nets (nnU-Net), Attention-U-Nets (Oktay et al. 2018) and SegResNets (Litjens et al. 2017), and their IB-extensions, as these networks had the highest accuracy in our experiments. The 3D IB filters are modular, independent, and easily deployable to any existing U-Net architecture. Our extension of SOTA U-Nets shows an increased performance in automatic organ segmentation from 3D MR and CT images and superior robustness for small datasets.

**In summary our paper:** (1) Introduces novel 3D inductive bias (IB) and shows how to use them in U-Net variations for optimal performance. (2) Extends nnU-Nets, Attention-U-Nets and SegResNets with the above IB and shows superior accuracy and robustness on datasets of multiple organs with different modalities.

## Related Work

### U-Net Variations.

This paper is mainly concerned with U-Nets (Ronneberger, Fischer, and Brox 2015; Çiçek et al. 2016) and their variations (Isensee et al. 2021; Oktay et al. 2018; Myronenko 2019; Milletari, Navab, and Ahmadi 2016), as they are the most popular biomedical-segmentation architecture in recent times. U-Nets have an encoder-decoder structure, where the encoder acts as a classifier identifying key features. In contrast, the decoder reconstructs the image from its low-dimensional discriminative features to its original pixel-level space. One of the variants named V-Net (Milletari, Navab, and Ahmadi 2016) replaces the U-Nets pooling layers with down/up convolutions for smaller memory footprint during training and introduce skip connections within every encoder block to improve convergence and learn residual functions. An alternative called Attention-U-Net (Oktay et al. 2018) employs an attention-gate module to automatically

learn to emphasize target structures of varying shapes and sizes.

SegResNet (Myronenko 2019) is another variation of the U-Net that has a segmentation architecture similar to V-Nets, but in addition uses a variational auto-encoder (VAE) branch. A VAE branch reconstructs the input image in order to regularize the shared decoder and impose additional constraints on its layers. On the other hand, the nnU-Net framework (Isensee et al. 2021) provides robust, and self-adapting networks based on 2D and 3D vanilla U-Nets, and a U-Net cascade. nnU-Net is the most widely used framework in medical image analysis after it achieved the first rank in multiple challenges.

### Medical-Image Segmentation

**Prostate-gland segmentation.** Over the past decade, significant research has been devoted to automatic segmentation of the prostate from MRIs (Gillespie et al. 2020). The original V-Net was trained on the PROMISE-12 dataset, where it achieved top results using dice loss and the model’s performance was determined by an overlap-based metric called dice similarity coefficient (DSC) (Milletari, Navab, and Ahmadi 2016). Ghavami et al. (2019) conducted a survey with four U-Net variants trained on a 3D MR dataset of 232 prostate patient volumes, and the results show that a statistically significant difference exists in the performances of these models. Tian et al. (2020) investigated an interactive segmentation approach by using a graph CNN to predict the prostate gland from the PROMISE-12 dataset. The nnU-Net framework (Isensee et al. 2021) achieved superior performance in prostate segmentation from PROMISE-12 and prostate-MSD datasets.

**Spleen segmentation.** Several studies have applied DL approaches to segment spleen from medical images (Altini et al. 2022). Gibson et al. (2018) proposed an encoder-decoder model called Dense V-Network for segmenting eight organs, including the spleen. The architecture of the Dense V-Network is similar to the U-Net, with the exception that they used dense blocks during the encoding path and bilinear upsampling in the decoding path. The nnU-Net framework (Isensee et al. 2021) again secured the top place for segmenting spleen from the MSD dataset. Inspired by the success of transformers for natural language processing, Hatamizadeh et al. (2022) proposed a new architecture called UNet Transformers (UNETR). While retaining the shape of the U-Net and without relying on convolutional layers for feature extraction, the UNETR uses a pure vision transformer as its encoder. The UNETR achieved good results on multi-organ segmentations, including the MSD-spleen segmentation task.

Based on previous works, it is evident that CNN based DL algorithms such as U-Nets are efficient in automatically segmenting organs from medical images.

### Biologically Inspired Architectures

**Vision models.** Initially, these models were inspired by neuroscience and psychology. In the meantime, both neuroscience and artificial intelligence (AI), particularly computer

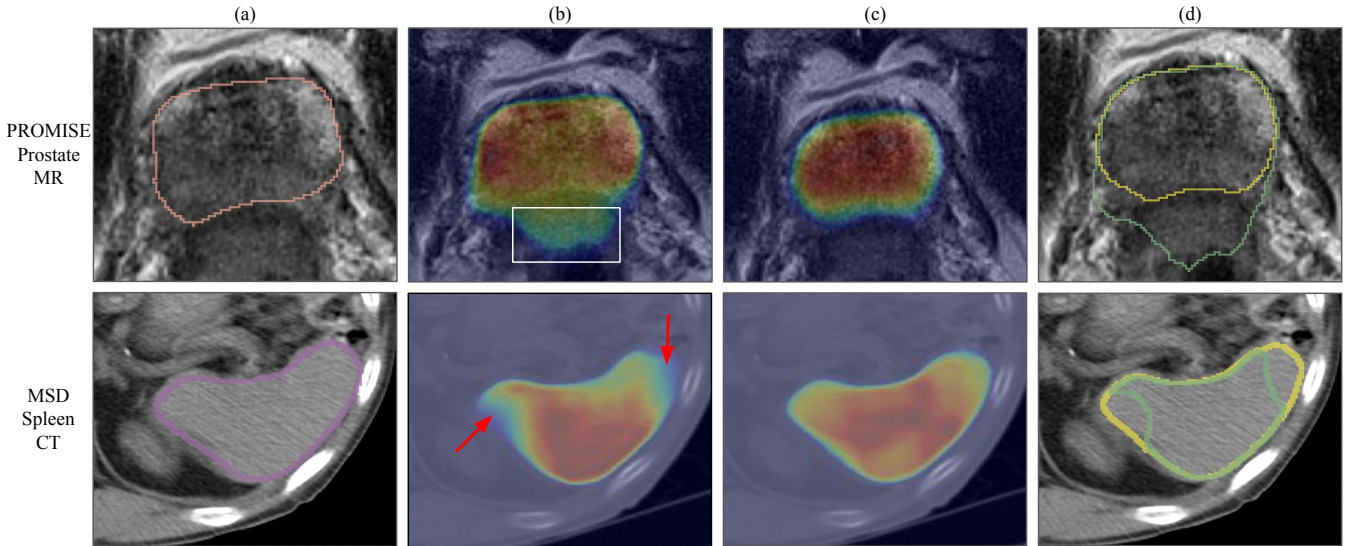


Figure 2: Comparison of the attention maps between the nnU-Net and IB-nnU-Net for volumes with a significant difference in accuracy. (a) The raw MR and CT images with annotated regions of interest – in PROMISE-prostate the red contour is the prostate, and in MSD-spleen the purple contour is the spleen. (b) The attention maps of nnU-Net for the given input volume. The white box in the attention map of nnU-Net for the PROMISE-prostate input signifies the area that should not have been activated. Whereas, the red arrows in the attention map for the MSD-spleen image denote sections missed by the model. (c) The attention maps of IB-nnU-Net for the given input volume. (d) Final predictions made by the networks for each task; green and yellow contours correspond to outputs of nnU-Net and IB-nnU-Net, respectively.

vision, have enormously progressed. However, most of today’s neural networks remained only loosely inspired by the visual system. The interaction between the fields has become less common, compared to the early age of AI, despite the importance of neuroscience in generating insightful ideas for AI (Brooks et al. 2012; Hassabis et al. 2017). One line of inquiry remained in the search for neuroscience-inspired enhancements of CNN architectures to increase their interpretability and robustness (Nayebi et al. 2018; Li et al. 2019; Dapello et al. 2020; Babaiee et al. 2021). In (Nayebi et al. 2018), local recurrence within cortical areas and long-range feedback from downstream areas to upstream areas are exploited in the design of novel recurrent CNNs, to increase interpretability and improve classification performance.

Li et al. (2019) proposed a new regularization technique of CNNs, which uses large-scale neuroscience data to learn more robust neural features in terms of representational similarity. In Dapello et al. (2020), a CNN architecture whose hidden layers better match with the primate primary visual cortex is proposed, which is more robust to adversarial attacks, such as imperceptibly small and explicitly crafted perturbations. Finally, the authors of Babaiee et al. (2021) added 2D On and Off center-surround parallel pathways present in the retina of vertebrates to CNNs and improved the robustness of image classification. This paper draws inspiration from U-Net variations and Babaiee et al. (2021) to design a medical-image segmentation architecture that can learn accurate and robust prostate segmentation from small 3D medical datasets.

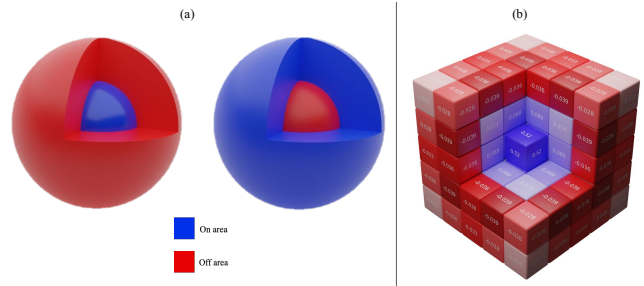


Figure 3: Different geometrical representations of the IB kernels. (a) Spherical On and Off 3D center-surround receptive fields. (b) The 3D IB-On cubic kernel. The 3D-IB Off cubic kernel is complimentary; all its signs are inverted.

### Inductive Biases in U-Net Variations

This section first shows how we compute the two 3D IB kernels. We then discuss how to extend the architecture of U-Net variations with the two inductive-bias kernels.

#### The Design of the 3D-IB Kernels

Receptive fields in the primate retina are captured with a difference of two Gaussians (DoG) (Rodieck 1965). For 2D kernels, Equation 1 computes the center and surround weights (Kruizinga and Petkov 2000; Petkov and Visser 2005):

$$DoG_{\sigma,\gamma}(x, y) = \frac{A_c}{\gamma^2} e^{-\frac{x^2+y^2}{2\gamma^2\sigma^2}} - A_s e^{-\frac{x^2+y^2}{2\sigma^2}} \quad (1)$$

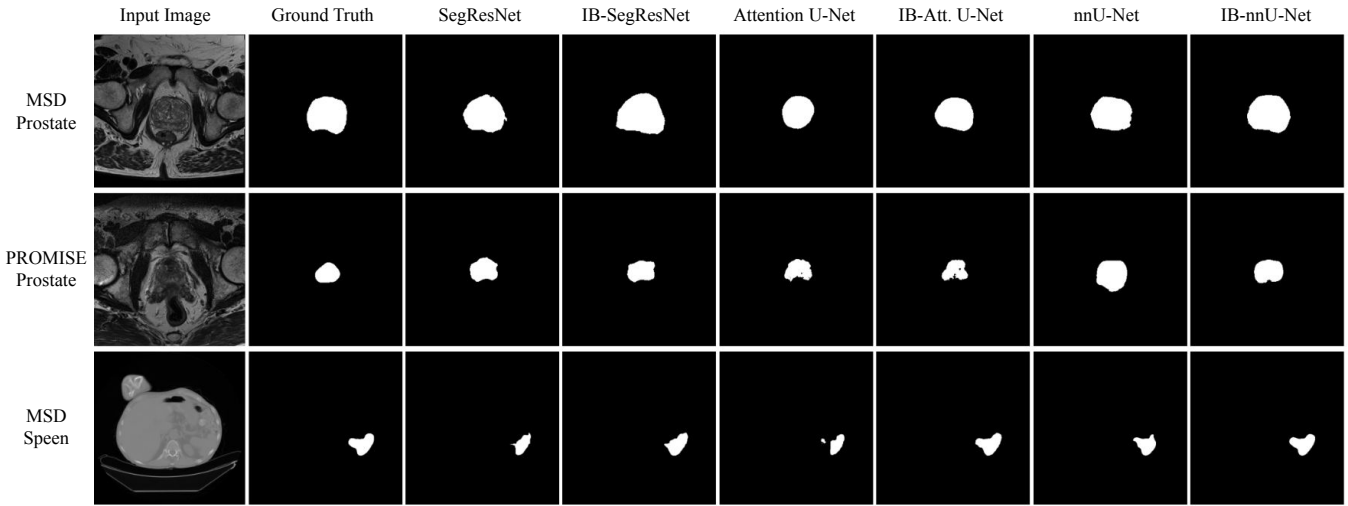


Figure 4: A qualitative accuracy comparison of vanilla U-Nets and their IB extended variants on the prostate and spleen segmentation tasks. IB-nnU-Nets perform the best.

where  $\gamma < 1$  is the ratio of the radius of the center to the one of the surround,  $\sigma$  is the variance of the Gaussian function, and  $A_c$  and  $A_s$  are the center and surround coefficients. To construct 3D-IB kernels, a naive way would be to use Equation 1 and repeat the kernels in the third axis. However, this approach would result in a cylindrical center-surround structure. A better way is to design a spherical structure, with excitatory center and an inhibitory surround. We therefore extend the 2D version as follows:

$$DoG_{\sigma,\gamma}(x, y, z) = \frac{A_c}{\gamma^3} e^{-\frac{x^2+y^2+z^2}{2\gamma^2\sigma^2}} - A_s e^{-\frac{x^2+y^2+z^2}{2\sigma^2}} \quad (2)$$

We set the absolute value of the sum of the negative and positive weights to be equal to an arbitrary value  $c \geq 1$ . This ensures the proper balance between excitation and inhibition, and the kernel weights will be large enough.

$$[DoG_{\sigma,\gamma}(x, y, z)]^+ dxdydz = c, \quad (3)$$

$$[DoG_{\sigma,\gamma}(x, y, z)]^- dxdydz = -c \quad (4)$$

By setting the sum of negative and positive values to the same value, the coefficients  $A_c$  and  $A_s$  will be equal in the infinite continuous case. To show that this result holds, we can write the DoG equation in polar coordinates:

$$\int_0^{r_s} \int_0^\pi \int_0^{2\pi} r^2 \sin(\varphi) \left( \frac{A_c}{\gamma^3} e^{-\frac{r^2}{2\gamma^2\sigma^2}} - A_s e^{-\frac{r^2}{2\sigma^2}} \right) d\theta d\varphi dr \quad (5)$$

where  $r$  is the radius of the central sphere. We can calculate the integral when  $r \rightarrow \infty$ , and by knowing that the sum of positive and negative weights is zero, we have:

$$\frac{2\sqrt{2}\pi^{\frac{3}{2}}}{\left(\frac{1}{\sigma^2}\right)^{\frac{3}{2}}} (A_c - A_s) = 0 \Rightarrow A_c = A_s \quad (6)$$

Assuming that the values of the coefficients are still close enough in the finite discrete case as well, we can approximate the variance of the Gaussians as follows:

$$\sigma \approx \frac{r}{\gamma} \sqrt{\frac{1-\gamma^2}{-6 \ln \gamma}} \quad (7)$$

### The Architecture of the Second Encoder Block

We used Equation 2 to calculate the fixed kernel weights for the On and Off (identical equation, but with signs inverted) convolutions. Note that we only needed to determine the kernel size ( $k$ ), the ratio of the radius of the center to surround, and the sum of positive and negative values to compute the fixed kernels. Figure 3 shows the  $5 \times 5 \times 5$  On kernel that we use in our experiments. Here we set  $\gamma = 2/3$  and  $r = 3$ . For a given input  $\chi$ , we calculate the On and Off responses by convolving  $\chi$  with the computed kernels separately:

$$\begin{aligned} \chi_{\text{On}}[x, y, z] &= (\chi * +DoG[r, \gamma, c])[x, y, z] \\ \chi_{\text{Off}}[x, y, z] &= (\chi * -DoG[r, \gamma, c])[x, y, z] \end{aligned} \quad (8)$$

We extended a 3D U-Net segmentation variation to a 3D IB-U-Net variation by changing its second encoder block to a 3D IB encoder block with  $k = 5$ , as shown in Figure 1. Through extensive experimentation, we found out that this IB extension results in the best accuracy and robustness on the chosen small-sized datasets. For instance, initially the input to IB layers was the outputs of the max-pooling layers, but the results improved only by an insignificant margin. We also used different values for the IB parameters, such as  $\gamma$  and  $r$ , thus creating kernels of different sizes. The use of even shaped kernels for convolution operation requires extra padding, and since this introduces artificial values, we restricted our design to kernels with odd shapes ( $k = 3, 5, 7, 9$ ). When using a kernel size of 3 ( $r = 1$ ,  $\gamma = 1/2$ ), the performance improved, but it was not always guaranteed. For larger kernel sizes such as  $k = 7$  ( $r = 3$ ,  $\gamma = 3/4$ ) and  $k = 9$  ( $r = 4$ ,  $\gamma = 4/5$ ), there was a large increase in the number of network parameters and training time with an insignificant margin of improvement (less than 0.1%) as compared to when  $k = 5$ .

In other scenarios, we added the IB layers in the second decoder block to maintain a degree of symmetry in the networks. However, this did not prove beneficial, as it helped

Table 1: Robustness of U-Net variants on the MSD-prostate dataset using DSC metric.

Dataset Name	Subsample Size	Model Name	No-Noise	Gaussian Blur Noise, $\sigma = 2$	Random Gaussian Noise, $\sigma = 45$
MSD-prostate	8	SegResNet	$0.555 \pm 0.337$	$0.513 \pm 0.319$	$0.540 \pm 0.225$
		IB-SegResNet	$0.560 \pm 0.231$	$0.555 \pm 0.214$	$0.526 \pm 0.303$
		Attention-U-Net	$0.456 \pm 0.289$	$0.153 \pm 0.198$	$0.520 \pm 0.308$
		IB-Att-U-Net	$0.657 \pm 0.109$	$0.609 \pm 0.101$	$0.627 \pm 0.112$
		nnU-Net	$0.705 \pm 0.095$	$0.673 \pm 0.105$	$0.704 \pm 0.098$
		IB-nnU-Net	<b><math>0.720 \pm 0.071</math></b>	<b><math>0.690 \pm 0.100</math></b>	<b><math>0.716 \pm 0.077</math></b>
MSD-prostate	16	SegResNet	$0.705 \pm 0.251$	$0.464 \pm 0.301$	$0.704 \pm 0.261$
		IB-SegResNet	$0.754 \pm 0.206$	$0.591 \pm 0.257$	$0.733 \pm 0.214$
		Attention-U-Net	$0.682 \pm 0.261$	$0.144 \pm 0.266$	$0.665 \pm 0.273$
		IB-Att-U-Net	$0.779 \pm 0.078$	$0.742 \pm 0.105$	$0.777 \pm 0.076$
		nnU-Net	$0.804 \pm 0.073$	$0.758 \pm 0.095$	$0.782 \pm 0.087$
		IB-nnU-Net	<b><math>0.821 \pm 0.063</math></b>	<b><math>0.789 \pm 0.085</math></b>	<b><math>0.793 \pm 0.076</math></b>
MSD-prostate	24	SegResNet	$0.805 \pm 0.181$	$0.672 \pm 0.230$	$0.733 \pm 0.264$
		IB-SegResNet	$0.808 \pm 0.188$	$0.685 \pm 0.220$	$0.790 \pm 0.193$
		Attention-U-Net	$0.816 \pm 0.119$	$0.478 \pm 0.341$	$0.773 \pm 0.159$
		IB-Att-U-Net	$0.819 \pm 0.113$	$0.594 \pm 0.314$	$0.776 \pm 0.202$
		nnU-Net	$0.823 \pm 0.065$	$0.803 \pm 0.097$	$0.816 \pm 0.087$
		IB-nnU-Net	<b><math>0.831 \pm 0.042</math></b>	<b><math>0.819 \pm 0.079</math></b>	<b><math>0.822 \pm 0.071</math></b>

for some scans but made some other volumetric segmentation results worse. In addition, we created networks where the IB layers were placed in all the encoder blocks, not just in the second encoder block. By doing this, we not only introduced more parameters, but our models started overfitting as well. Therefore, we decided to utilize the IB kernels only in the second encoder block.

To add the On and Off IBs to the second convolution block, we first divided the convolution layers of the block into two parallel pathways, with half of the filters in the original layer in each divided convolution. This architecture mimics the so-called On and Off pathways in the retina. We added the 3D On and Off convolved inputs of the block to the activation maps of the first convolution layers of the pathways before max-pooling, such that we do not lose information. This required the use of a stride of two for the IBs. We experimentally observed that adding the IBs after max-pooling and with a stride of one leads to worse results. Finally, we concatenated the activation maps of the last layers on the pathways, resulting in the outputs with the same shapes as the outputs of the original block.

## Materials and Methods

### U-Net Variations Used in Our Experiments

To explore the merit of IBs in U-Nets, we first examined the accuracy and robustness of all variations mentioned in Section and their extension. Attention-U-Nets and SegRes-Nets introduced novel multi-view and multi-scale functions, which enhanced the receptive fields of the networks and reduced bottlenecks during computation, essentially shortening the time required to converge. Furthermore, these architectures showed excellent performances on the public dataset. Therefore, we proceeded to further benchmark these

two architectures in our framework. However, we excluded the V-Net from this paper, as the SegResNet has a similar structure as that of the former model. Moreover, the SegResNet improves on the V-Net by introducing a VAE branch. While all variations benefited from the IB extension, nnU-Nets, Attention-U-Nets and SegResNets performed best. nnU-Nets, Attention-U-Nets and SegResNets were extended with 3D-IB filters of kernel sizes  $k = 5$ . The resulting new networks are called as follows: IB-nnU-Net, IB-Att-U-Net and IB-SegResNet respectively.

### Datasets

In all our experiments concerning the prostate organ, we utilized two MRI datasets from two different public sources: PROMISE-12 and MSD-prostate.

**PROMISE-12:** The PROMISE-12 dataset offers 80 (training=50, testing=30) volumes of transversal T2-weighted MRIs of the prostate. This dataset was selected as it is a compilation of scans collected from multiple centres and vendors with different acquisition protocols. Due to this fact, there is a heterogeneity in the voxel-spacings and the slice thickness of the volumes.

**MSD-prostate:** The MSD-prostate dataset comprises of 48 (training=32, testing=16) multimodal (T2, ADC) 3D MRI samples. We only considered the T2-weighted modality as they provide most of the necessary anatomical information, whereas the ADC modality is often considered for tumour characterization/segmentation. Furthermore, the ground-truth labels of the original MSD-prostate dataset are separated into annotations of the central prostate gland and the peripheral zone. We combined the two regions into one label such that all U-Net variations could learn a binary im-

Table 2: Robustness of U-Net variants on the PROMISE-12 dataset using DSC metric.

Subsample Size	Model Name	No-Noise	Gaussian Blur Noise, $\sigma = 2$	Random Gaussian Noise, $\sigma = 45$
8	SegResNet	0.559 $\pm$ 0.267	0.392 $\pm$ 0.311	0.510 $\pm$ 0.326
	IB-SegResNet	0.624 $\pm$ 0.214	0.495 $\pm$ 0.246	0.639 $\pm$ 0.189
	Attention-U-Net	0.512 $\pm$ 0.325	0.079 $\pm$ 0.123	0.508 $\pm$ 0.317
	IB-Att-U-Net	0.674 $\pm$ 0.104	0.623 $\pm$ 0.199	0.662 $\pm$ 0.112
	nnU-Net	0.722 $\pm$ 0.136	0.704 $\pm$ 0.175	0.721 $\pm$ 0.146
	IB-nnU-Net	<b>0.735 <math>\pm</math> 0.127</b>	<b>0.713 <math>\pm</math> 0.159</b>	<b>0.719 <math>\pm</math> 0.135</b>
16	SegResNet	0.618 $\pm$ 0.267	0.603 $\pm$ 0.301	0.611 $\pm$ 0.268
	IB-SegResNet	0.705 $\pm$ 0.213	0.650 $\pm$ 0.297	0.678 $\pm$ 0.224
	Attention-U-Net	0.582 $\pm$ 0.298	0.241 $\pm$ 0.304	0.589 $\pm$ 0.273
	IB-Att-U-Net	0.622 $\pm$ 0.251	0.461 $\pm$ 0.349	0.617 $\pm$ 0.261
	nnU-Net	0.759 $\pm$ 0.155	0.740 $\pm$ 0.169	<b>0.751 <math>\pm</math> 0.160</b>
	IB-nnU-Net	<b>0.779 <math>\pm</math> 0.146</b>	<b>0.743 <math>\pm</math> 0.158</b>	0.738 $\pm$ 0.175
24	SegResNet	0.645 $\pm$ 0.234	0.532 $\pm$ 0.244	0.594 $\pm$ 0.296
	IB-SegResNet	0.768 $\pm$ 0.130	0.596 $\pm$ 0.237	0.723 $\pm$ 0.239
	Attention-U-Net	0.690 $\pm$ 0.234	0.449 $\pm$ 0.302	0.640 $\pm$ 0.245
	IB-Att-U-Net	0.737 $\pm$ 0.162	0.487 $\pm$ 0.307	0.645 $\pm$ 0.288
	nnU-Net	0.803 $\pm$ 0.104	0.794 $\pm$ 0.125	0.800 $\pm$ 0.124
	IB-nnU-Net	<b>0.811 <math>\pm</math> 0.095</b>	<b>0.800 <math>\pm</math> 0.120</b>	<b>0.802 <math>\pm</math> 0.108</b>

age segmentation. Similar to the PROMISE-12, the MSD-prostate dataset was selected as it has a significant amount of inter-subject variability.

**MSD-spleen:** The spleen dataset consists of 61 (training=41, testing=20) monomodal 3D CT samples. We wanted to work with this dataset because of two reasons; first, it has a small sample size, and second, we wanted to check the potential of the IB kernels when handling CT images with large variations in their field-of-view.

### Implementation of our framework

Other than extending the networks with the IB kernels, we did not make any alterations to the original networks, including the convolution and normalization layers (Ioffe and Szegedy 2015), activation functions, and dropout layers and probabilities. All the necessary source code for the framework was implemented in PyTorch (Paszke et al. 2019).

The volumes in the three datasets have varying voxel spacings, and CNNs disregard this information while operating on the voxel grids. To handle this heterogeneity in the datasets, all the images and their corresponding ground truth labels were resampled to the target voxel spacings of their respective datasets:  $0.6125 \times 0.6125 \times 2.2mm^3$  for PROMISE-12,  $0.625 \times 0.625 \times 3.6mm^3$  for the MSD-prostate and  $0.79 \times 0.79 \times 1.6mm^3$  for MSD-spleen. We employed tri-linear and nearest-neighbour interpolation to resample the images and annotated labels, respectively. In most biomedical cases, we cannot fit the complete image into the GPU due to the large sizes. For that reason, 3D patches of foreground and background were randomly sampled with equal probabilities. The shape of the sampled patches were:  $192 \times 192 \times 16$  voxels for the PROMISE-

12 dataset,  $288 \times 288 \times 16$  for the MSD-prostate set, and  $192 \times 192 \times 96$  for the spleen dataset.

The intensity values of the MR scans were linearly scaled using a standard (z-score) normalization such that the mean value and standard deviation of the transformed data equalled to 0 and 1, respectively. As for CT images, the first 0.5 and 99.5 percentiles of the foreground voxels were clipped, and then normalized using the global foreground mean and standard deviation. To synthesize additional data during training, the data pipeline carried out augmentations, such as elastic deformations, gamma correction, random Gaussian noise, Gaussian blur, rotations, and scaling. Throughout all the experiments, we used the Adam optimization algorithm with an initial learning rate of  $1e-04$  that decays using a polynomial scheduler (Myronenko 2019) for 500 epochs. We used L2 regularization on the convolution kernel parameters with a weight of  $1e-05$ . The gradient updates were evaluated with a mini-batch size of two for all the datasets.

**Loss functions:** We utilized a combination of two-loss functions; Binary Cross-Entropy loss ( $L_{BCE}$ ) and Sørensen-Dice Loss ( $L_{dice}$ ) (Sudre et al. 2017) together make BCE-dice loss ( $L_{BCE-dice}$ ) (Milletari, Navab, and Ahmadi 2016) to train the models. This compound loss is defined over all semantic classes and is less sensitive to class imbalance, as demonstrated experimentally in Ma et al. (2021). The equations for BCE-dice loss are given as follows:

$$L_{BCE} = -\frac{1}{N} \cdot \sum_{i=1}^N g_i \cdot \log(p_i) + (1 - g_i) \cdot \log(1 - p_i) \quad (9)$$

$$L_{dice} = 1 - \frac{2 \cdot \sum_{i=1}^N p_i g_i}{\sum_{i=1}^N p_i^2 + \sum_{i=1}^N g_i^2} \quad (10)$$

Table 3: Robustness of U-Net variants on the MSD-spleen dataset using DSC metric.

Subsample Size	Model Name	No-Noise	Gaussian Blur Noise, $\sigma = 2$	Random Gaussian Noise, $\sigma = 45$
8	SegResNet	0.601 $\pm$ 0.311	0.605 $\pm$ 0.304	0.593 $\pm$ 0.294
	IB-SegResNet	0.621 $\pm$ 0.271	0.618 $\pm$ 0.285	0.616 $\pm$ 0.274
	Attention-U-Net	0.615 $\pm$ 0.293	0.603 $\pm$ 0.303	0.611 $\pm$ 0.300
	IB-Att-U-Net	0.630 $\pm$ 0.235	0.612 $\pm$ 0.289	0.615 $\pm$ 0.275
	nnU-Net	0.652 $\pm$ 0.247	0.628 $\pm$ 0.244	0.650 $\pm$ 0.236
	IB-nnU-Net	<b>0.665 <math>\pm</math> 0.233</b>	<b>0.631 <math>\pm</math> 0.241</b>	<b>0.659 <math>\pm</math> 0.234</b>
16	SegResNet	0.704 $\pm$ 0.197	0.661 $\pm$ 0.211	0.679 $\pm$ 0.201
	IB-SegResNet	0.715 $\pm$ 0.183	0.704 $\pm$ 0.190	0.711 $\pm$ 0.178
	Attention-U-Net	0.728 $\pm$ 0.171	0.719 $\pm$ 0.180	0.720 $\pm$ 0.184
	IB-Att-U-Net	0.739 $\pm$ 0.168	0.722 $\pm$ 0.181	0.734 $\pm$ 0.169
	nnU-Net	<b>0.754 <math>\pm</math> 0.152</b>	0.730 $\pm$ 0.168	<b>0.746 <math>\pm</math> 0.149</b>
	IB-nnU-Net	0.751 $\pm$ 0.154	<b>0.732 <math>\pm</math> 0.166</b>	0.741 $\pm$ 0.150
24	SegResNet	0.818 $\pm$ 0.118	0.776 $\pm$ 0.146	0.765 $\pm$ 0.148
	IB-SegResNet	0.819 $\pm$ 0.109	0.799 $\pm$ 0.121	0.786 $\pm$ 0.135
	Attention-U-Net	0.841 $\pm$ 0.088	0.824 $\pm$ 0.114	0.817 $\pm$ 0.122
	IB-Att-U-Net	0.843 $\pm$ 0.080	0.833 $\pm$ 0.091	0.829 $\pm$ 0.106
	nnU-Net	0.868 $\pm$ 0.067	0.840 $\pm$ 0.102	<b>0.852 <math>\pm</math> 0.093</b>
	IB-nnU-Net	<b>0.872 <math>\pm</math> 0.067</b>	<b>0.842 <math>\pm</math> 0.100</b>	0.851 $\pm$ 0.093

$$L_{\text{BCE-dice}} = L_{\text{BCE}} + L_{\text{dice}} \quad (11)$$

$N$  is the number of voxels,  $p_i$  and  $g_i$  denote the prediction and ground-truth label at voxel  $i$  respectively, for an image.

In the validation phase, neither patch sampling was done nor any augmentations were applied, rather only the appropriate normalization techniques were applied to the full image. Next, to predict the label, a sliding window technique was used with an overlap of  $1/2$  in each dimension, and the window shape was the set to the training patch size. The state values of the model configuration with the highest metric value was saved and later used for inference. The models were evaluated based on the DSC metric (Dice score), as it exhibits a low overall bias in 3D medical image segmentation tasks (Taha and Hanbury 2015; Maier-Hein et al. 2022). The Dice score is defined in equation 12, where  $\epsilon$  is the smoothing factor with a value of  $10^{-6}$ .

$$\text{DSC} = \frac{2 * \sum_{i=1}^N p_i g_i + \epsilon}{\sum_{i=1}^N p_i^2 + \sum_{i=1}^N g_i^2 + \epsilon} \quad (12)$$

Once the training was finished, first the voxel-wise semantic predictions were generated using the best network parameters, and then the labels were resampled to their original spacings. Next, we retrieved the desired region by taking the largest connected component (apart from the background) of the resultant resampled volume. The inference step ended after the final metric values were calculated, and the detailed results were saved.

## Experiments and Results

The proposed 3D IB filters are modular and independent of the network’s architecture, allowing them to be easily deployed to image segmentation tasks. Unfortunately, the ground-truth labels for the testing images are not publicly

available for any of the datasets mentioned in Section . Consequently, to analyze the capabilities of the networks, we conducted two kinds of CV using the 50 MR volumes, 32 MR images and 41 CT scans from the PROMISE-12, MSD-prostate, and MSD-spleen datasets, respectively. First, we implemented 8-fold CV by randomly sampling three subsets each from the datasets. The sample size was chosen such that it would be a factor of 8, hence, the number of volumes in each sub-sample was 8, 16 and 24 respectively. This made sure that we could investigate the capabilities of our IB extensions on small-sized datasets. Second, we investigated the models for all available volumes in the three datasets for completeness using 5-fold CV. For the nnU-Net framework, we extended the U-Net of the nnU-Net with the IB kernels, and then followed the steps detailed in Isensee et al. (2021). We ran our experiments on an NVIDIA Titan RTXs with 24 GB memory. The CV method for a single network on one dataset was completed in four and six days with our framework and when using the nnU-Net framework, respectively. We acknowledge that training models for a long period could possibly negatively impact the environment, but this can be mitigated in future works by training the best model presented in this paper with a 5-fold CV method.

Initially, we examined the accuracy and robustness of the SegResNets, Attention-U-Nets, nnU-Nets and their IB extensions on the original volumes. Figure 4 illustrates a few of the qualitative examples by comparing the predictions of the U-Net variations and their IB extensions, and it is evident that the IB extensions are more accurate than the original U-Nets. The IB-nnU-Net attained the highest result. In the next stage, we corrupted the original volumes by adding two types of noise: Gaussian blur and random Gaussian noise. We used the Torchio package (Pérez-García, Sparks, and Ourselin 2021) to create the noisy datasets.

Table 4: Accuracy of U-Net variants and their IB extensions on the full datasets without any artifacts.

Model Name	MSD-prostate (32)	PROMISE-12 (50)	Spleen dataset (41)
SegResNet	0.841 $\pm$ 0.085	0.885 $\pm$ 0.035	0.901 $\pm$ 0.083
IB-SegResNet	<b>0.844 <math>\pm</math> 0.078</b>	<b>0.888 <math>\pm</math> 0.033</b>	<b>0.902 <math>\pm</math> 0.080</b>
Attention-U-Net	0.835 $\pm$ 0.075	0.891 $\pm$ 0.033	0.938 $\pm$ 0.062
IB-Att-U-Net	<b>0.845 <math>\pm</math> 0.066</b>	<b>0.892 <math>\pm</math> 0.032</b>	<b>0.941 <math>\pm</math> 0.058</b>
nnU-Net	0.882 $\pm$ 0.118	0.890 $\pm$ 0.101	0.966 $\pm$ 0.044
IB-nnU-Net	<b>0.895 <math>\pm</math> 0.042</b>	<b>0.902 <math>\pm</math> 0.036</b>	<b>0.970 <math>\pm</math> 0.017</b>

### Robustness Evaluation on Small Subsets

Tables 1, 2 and 3 summarise our accuracy and robustness results for SegResNets, Attention-U-Nets, nnU-Nets and their IB extensions. The best performance is emphasized in boldface. The key takeaway is that IB extensions are more performant. As demonstrated by Table 1, the IB extensions always have superior performance on the MSD-prostate dataset. Additionally, in Tables 2 and 3, a similar observation is also true for the PROMISE-12 and the spleen dataset, with a few exceptions: the nnU-Net for 16 and 24 subsamples. In these cases, the lower performance of the IB extension could be attributed to the presence of outliers. Please note, however, that the variance in these two cases is relatively high. Thus, the results for the IB extensions are still within the same range as the ones for original nnU-Net. In general, the variance of the vanilla U-Net variants is larger in these tables than the one of their IB extensions.

### Robustness Evaluation on Full Dataset

For completeness, in Table 4 we provide the DSC-accuracy results of SegResNets, Attention-U-Nets, nnU-Nets and their IB-extensions, for all available volumes in the three datasets. Similar to Tables 1, 2 and 3, the IB-extensions are performing better for full datasets. However, the performance improvement is not that significant any more. In other words, the smaller the dataset, the more rectifying is the addition of IB to the U-Nets. This is true in general for machine learning (ML): the smaller the dataset, the more important is the ML algorithm.

### Cylindrical versus Spherical IB kernels

The extension of the IB kernel from 2D to 3D is non-trivial. If we assume that the 3D IB kernel is simply the repeated stacking of the 2D kernel on top of one another (along the z-axis, with each slice having the same weights), then this leads to a cylindrical kernel. Table 5 shows the performance of the spherical kernel against the cylindrical kernels for the Attention U-Net. As one can see, our spherical kernel outperforms other variants, while the cylindrical versions are inferior compared to the original Attention U-Net. The cylindrical kernels make mistakes when considering 3D contours; therefore, it is crucial to make modifications. Moreover, Babaie et al. (2021) used natural images to evaluate the performance of the 2D IB kernels, and the kernels that work for 2D may not necessarily be suitable in the 3D setting. The properties of 3D medical images, such as the voxel

Table 5: Comparison of robustness among Attention U-Net, cylindrical IB-attention U-Nets ( $k = 3$  and  $k = 5$ ), and spherical IB-attention U-Net ( $k = 5$ ) on subsample size 8 of the PROMISE-12 dataset using the DSC metric. To be added in the final version.

Model Name	DSC ( $\uparrow$ )
Attention-U-Net	0.512 $\pm$ 0.325
Cyl IB-Att. U-Net (k3)	0.438 $\pm$ 0.358
Cyl IB-Att. U-Net (k5)	0.445 $\pm$ 0.336
IB-Att. U-Net (k5)	<b>0.674 <math>\pm</math> 0.104</b>

Table 6: Comparison of robustness amongst nnU-Net and its IB-extended U-Nets (k3, k5, k7 and k9) on the full PROMISE-12 dataset using the DSC metric. We will add it in the final version.

Model Name	DSC ( $\uparrow$ )
nnU-Net	0.890 $\pm$ 0.101
IB-nnU-Net ( $k = 3, r = 1, \gamma = 1/2$ )	0.887 $\pm$ 0.086
IB-nnU-Net ( $k = 5, r = 2, \gamma = 2/3$ )	<b>0.902 <math>\pm</math> 0.036</b>
IB-nnU-Net ( $k = 7, r = 3, \gamma = 3/4$ )	0.898 $\pm$ 0.055
IB-nnU-Net ( $k = 9, r = 4, \gamma = 4/5$ )	0.895 $\pm$ 0.058

spacings, matrix directions, origins etc., produce significant artifacts that the cylindrical kernels cannot handle well.

### Different parameters of IB kernels

The section on the architecture of the second encoder block discusses the performances of the various IB-extended U-Net architectures, such as U-Nets with multiple IB blocks; however, their performances were not satisfactory. We also conducted experiments with different  $k$ ,  $r$ , and  $\gamma$ , and the quantitative results are given in Table 6. It is clear that the IB-nnU-Net variant with parameter values of  $k = 5$ ,  $r = 2$ , and  $\gamma = 2/3$  is the best performing version

### Discussion and Conclusion

We introduced two new 3D kernels, inspired by the on and off center-surround pathways originating in the vertebrate retina, and we proposed a procedure to compute the kernel weights. We showed how to extend the second encoder block of U-Net variations, using these precomputed kernels as inductive biases, helping to scrutinize and delineate anatom-

Table 7: Accuracy of nnU-Net and IB-nnU-Net on the full datasets without any artifacts using the HD95 (in mm) metric. To be added.

Dataset Name	Model Name	HD95 in mm ( $\downarrow$ )
MSD-prostate	nnU-Net	15.078 $\pm$ 75.203
	IB-nnU-Net	<b>1.738 <math>\pm</math> 1.122</b>
PROMISE-12	nnU-Net	9.735 $\pm$ 59.565
	IB-nnU-Net	<b>1.237 <math>\pm</math> 0.556</b>
MSD-spleen	nnU-Net	1.640 $\pm$ 4.708
	IB-nnU-Net	<b>1.189 <math>\pm</math> 1.914</b>

ical structures of 3D images with increased accuracy. Although our proposed 3D-IB-encoder block slightly increases the number of training parameters of the networks, the modification steps are effortless, and it requires minimal computational overhead.

The IB kernels can help in scenarios where the dataset has at least two outliers (very different samples). In this case, the other models have difficulties in segmenting the region of interest (ROI). This is evident in Figures 2 and 4, as well as in Table 4, where the standard deviation of the best performing IB-nnU-Net is smaller than that of the second place nnU-Net. The marginal improvement of performances in Table 3 could be due to sampling very similar volumes from the spleen task without any outliers. In the full MSD-spleen dataset, the ROI is so large that when the model prediction is incorrect by a significant margin, the DSC metric may not capture this distinction accurately. Therefore, in Table 7 we have listed the segmentation performances of the nnU-Net and IB-nnU-Net, respectively, using a surface distance metric called the 95th percentile Hausdorff distance (HD95).

Robustness to distribution shifts is a crucial attribute of any deep neural network, and it is of even higher importance for networks used in critical domains like bio-medical tasks. Our experiments on multiple organ segmentation tasks with our baseline networks and their IB extensions show notable enhancements in the performance of the IB-equipped networks. Furthermore, our robustness experiments demonstrate the superior performance of IB extended networks. Figure 2 shows that the IB extension improves a network’s focus on critical structures. In conclusion, the proposed method could make the 3D-IB kernels a favourable approach to achieve accurate results in 3D medical image segmentation tasks with small sized datasets.

## Acknowledgements

This research was funded in part by the Austrian Science Fund (FWF): I 4718, and the Federal Ministry of Education and Research (BMBF) Germany, under the frame of ERA PerMed. Z. B. was supported by the Doctoral College Resilient Embedded Systems, which is run jointly by the TU Wien’s Faculty of Informatics and the UAS Technikum Wien.

## Code and Data Availability

All code and data are included in [https://github.com/Shrajan/IB\\_U\\_Nets](https://github.com/Shrajan/IB_U_Nets).

## References

- Altini, N.; Prencipe, B.; Casciarano, G. D.; Brunetti, A.; Brunetti, G.; Triggiani, V.; Carnimeo, L.; Marino, F.; Guerriero, A.; Villani, L.; Scardapane, A.; and Bevilacqua, V. 2022. Liver, kidney and spleen segmentation from CT scans and MRI with deep learning: A survey. *Neurocomputing*, 490: 30–53.
- Antonelli, M.; Reinke, A.; Bakas, S.; Farahani, K.; AnnetteKopp-Schneider; Landman, B. A.; Litjens, G.; Menze, B.; Ronneberger, O.; Summers, R. M.; van Ginneken, B.; Bilello, M.; Bilic, P.; Christ, P. F.; Do, R. K. G.; Gollub, M. J.; Heckers, S. H.; Huisman, H.; Jarnagin, W. R.; McHugo, M. K.; Napel, S.; Pernicka, J. S. G.; Rhode, K.; Tobon-Gomez, C.; Vorontsov, E.; Huisman, H.; Meakin, J. A.; Ourselin, S.; Wiesenfarth, M.; Arbelaez, P.; Bae, B.; Chen, S.; Daza, L.; Feng, J.; He, B.; Isensee, F.; Ji, Y.; Jia, F.; Kim, N.; Kim, I.; Merhof, D.; Pai, A.; Park, B.; Perslev, M.; Rezaifar, R.; Rippel, O.; Sarasua, I.; Shen, W.; Son, J.; Wachinger, C.; Wang, L.; Wang, Y.; Xia, Y.; Xu, D.; Xu, Z.; Zheng, Y.; Simpson, A. L.; Maier-Hein, L.; and Cardoso, M. J. 2021. The Medical Segmentation Decathlon. *arXiv preprint arXiv:2106.05735*.
- Antonelli, M.; Reinke, A.; Bakas, S.; Farahani, K.; Kopp-Schneider, A.; Landman, B. A.; Litjens, G.; Menze, B.; Ronneberger, O.; Summers, R. M.; van Ginneken, B.; Bilello, M.; Bilic, P.; Christ, P. F.; Do, R. K. G.; Gollub, M. J.; Heckers, S. H.; Huisman, H.; Jarnagin, W. R.; McHugo, M. K.; Napel, S.; Pernicka, J. S. G.; Rhode, K.; Tobon-Gomez, C.; Vorontsov, E.; Meakin, J. A.; Ourselin, S.; Wiesenfarth, M.; Arbeláez, P.; Bae, B.; Chen, S.; Daza, L.; Feng, J.; He, B.; Isensee, F.; Ji, Y.; Jia, F.; Kim, I.; Maier-Hein, K.; Merhof, D.; Pai, A.; Park, B.; Perslev, M.; Rezaifar, R.; Rippel, O.; Sarasua, I.; Shen, W.; Son, J.; Wachinger, C.; Wang, L.; Wang, Y.; Xia, Y.; Xu, D.; Xu, Z.; Zheng, Y.; Simpson, A. L.; Maier-Hein, L.; and Cardoso, M. J. 2022. The Medical Segmentation Decathlon. *Nature Communications*, 13(1): 4128.
- Babaiee, Z.; Hasani, R.; Lechner, M.; Rus, D.; and Grosu, R. 2021. On-Off Center-Surround Receptive Fields for Accurate and Robust Image Classification. *Proceedings of the 38th International Conference on Machine Learning*, 139: 478–489.
- Brooks, R.; Hassabis, D.; Bray, D.; and Shashua, A. 2012. Turing centenary: Is the brain a good model for machine intelligence? *Nature*, 482: 462–3.
- Çiçek, Ö.; Abdulkadir, A.; Lienkamp, S. S.; Brox, T.; and Ronneberger, O. 2016. 3D U-Net: learning dense volumetric segmentation from sparse annotation. *International conference on medical image computing and computer-assisted intervention*, 424–432.
- Consortium, M. 2020. MONAI: Medical Open Network for AI.
- Dapello, J.; Marques, T.; Schrimpf, M.; Geiger, F.; Cox, D.; and DiCarlo, J. J. 2020. Simulating a Primary Visual Cortex

- at the Front of CNNs Improves Robustness to Image Perturbations. *Advances in Neural Information Processing Systems*, 33: 13073–13087.
- Ghavami, N.; Hu, Y.; Gibson, E.; Bonmati, E.; Emberton, M.; Moore, C. M.; and Barratt, D. C. 2019. Automatic segmentation of prostate MRI using convolutional neural networks: Investigating the impact of network architecture on the accuracy of volume measurement and MRI-ultrasound registration. *Medical Image Analysis*, 58.
- Gibson, E.; Giganti, F.; Hu, Y.; Bonmati, E.; Bandula, S.; Gurusamy, K.; Davidson, B.; Pereira, S. P.; Clarkson, M. J.; and Barratt, D. C. 2018. Automatic Multi-Organ Segmentation on Abdominal CT With Dense V-Networks. *IEEE Transactions on Medical Imaging*, 37(8): 1822–1834.
- Gillespie, D.; Kendrick, C.; Boon, I.; Boon, C.; Rattay, T.; and Yap, M. H. 2020. Deep learning in magnetic resonance prostate segmentation: A review and a new perspective. *arXiv preprint arXiv:2011.07795*.
- Goldenberg, S. L.; Nir, G.; and Salcudean, S. E. 2019. A new era: artificial intelligence and machine learning in prostate cancer. *Nature Reviews Urology*, 16(7): 391–403.
- Hassabis, D.; Kumaran, D.; Summerfield, C.; and Botvinick, M. 2017. Neuroscience-Inspired Artificial Intelligence. *Neuron*, 95(2): 245–258.
- Hatamizadeh, A.; Tang, Y.; Nath, V.; Yang, D.; Myronenko, A.; Landman, B.; Roth, H. R.; and Xu, D. 2022. Unetr: Transformers for 3d medical image segmentation. *Proceedings of the IEEE/CVF Winter Conference on Applications of Computer Vision*, 574–584.
- Ioffe, S.; and Szegedy, C. 2015. Batch Normalization: Accelerating Deep Network Training by Reducing Internal Covariate Shift. *Proceedings of the 32nd International Conference on Machine Learning*, 37: 448–456.
- Isensee, F.; Jaeger, P. F.; Kohl, S. A. A.; Petersen, J.; and Maier-Hein, K. H. 2021. nnU-Net: a self-configuring method for deep learning-based biomedical image segmentation. *Nature methods*, 18(2): 203–211.
- Krizhevsky, A.; Sutskever, I.; and Hinton, G. E. 2012. ImageNet Classification with Deep Convolutional Neural Networks. *Proceedings of the 25th International Conference on Neural Information Processing Systems - Volume 1*, 1097–1105.
- Kruizinga, P.; and Petkov, N. 2000. Computational model of dot-pattern selective cells. *Biological Cybernetics*, 83(4): 313–325.
- Li, Z.; Brendel, W.; Walker, E.; Cobos, E.; Muhammad, T.; Reimer, J.; Bethge, M.; Sinz, F.; Pitkow, Z.; and Tolias, A. 2019. Learning from brains how to regularize machines. *Advances in neural information processing systems*, 32.
- Litjens, G.; Kooi, T.; Bejnordi, B. E.; Setio, A. A. A.; Ciompi, F.; Ghafoorian, M.; van der Laak, J. A.; van Ginneken, B.; and Sánchez, C. I. 2017. A survey on deep learning in medical image analysis. *Medical Image Analysis*, 42: 60–88.
- Litjens, G.; Toth, R.; (van de Ven), W.; Hoeks, C.; Kerkstra, S.; (van Ginneken), B.; Vincent, G.; Guillard, G.; Birbeck, N.; Zhang, J.; Strand, R.; Malmberg, F.; Ou, Y.; Davatzikos, C.; Kirschner, M.; Jung, F.; Yuan, J.; Qiu, W.; Gao, Q.; Edwards, P. E.; Maan, B.; van-der Heijden, F.; Ghose, S.; Mitra, J.; Dowling, J.; Barratt, D.; Huisman, H.; and Madabhushi, A. 2014. Evaluation of prostate segmentation algorithms for MRI: The PROMISE12 challenge. *Medical Image Analysis*, 18(2): 359–373.
- Ma, J.; Chen, J.; Ng, M.; Huang, R.; Li, Y.; Li, C.; Yang, X.; and Martel, A. L. 2021. Loss odyssey in medical image segmentation. *Medical Image Analysis*, 71: 102035.
- Maier-Hein, L.; Reinke, A.; Christodoulou, E.; Glocker, B.; Godau, P.; Isensee, F.; Kleesiek, J.; Kozubek, M.; Reyes, M.; Riegler, M. A.; et al. 2022. Metrics reloaded: Pitfalls and recommendations for image analysis validation. *arXiv preprint arXiv:2206.01653*.
- Milletari, F.; Navab, N.; and Ahmadi, S.-A. 2016. V-Net: Fully Convolutional Neural Networks for Volumetric Medical Image Segmentation. *2016 Fourth International Conference on 3D Vision (3DV)*, 565–571.
- Myronenko, A. 2019. 3D MRI Brain Tumor Segmentation Using Autoencoder Regularization. *Brainlesion: Glioma, Multiple Sclerosis, Stroke and Traumatic Brain Injuries*, 311–320.
- Nayebi, A.; Bear, D.; Kubilius, J.; Kar, K.; Ganguli, S.; Sussillo, D.; DiCarlo, J. J.; and Yamins, D. L. 2018. Task-Driven Convolutional Recurrent Models of the Visual System. *Advances in Neural Information Processing Systems*, 31.
- Oktay, O.; Schlemper, J.; Folgoc, L. L.; Lee, M. C. H.; Heinrich, M. P.; Misawa, K.; Mori, K.; McDonagh, S. G.; Hammerla, N. Y.; Kainz, B.; Glocker, B.; and Rueckert, D. 2018. Attention U-Net: Learning Where to Look for the Pancreas. *Medical Imaging with Deep Learning*.
- Paszke, A.; Gross, S.; Massa, F.; Lerer, A.; Bradbury, J.; Chanan, G.; Killeen, T.; Lin, Z.; Gimelshein, N.; Antiga, L.; et al. 2019. Pytorch: An imperative style, high-performance deep learning library. *Advances in neural information processing systems*, 32.
- Petkov, N.; and Visser, W. T. 2005. Modifications of Center-Surround, Spot Detection and Dot-Pattern Selective Operators. Technical Report 2005-9-01, Institute of Mathematics and Computing Science, University of Groningen, Netherlands.
- Pérez-García, F.; Sparks, R.; and Ourselin, S. 2021. TorchIO: A Python library for efficient loading, preprocessing, augmentation and patch-based sampling of medical images in deep learning. *Computer Methods and Programs in Biomedicine*, 208: 106236.
- Rischke, H. C.; Nestle, U.; Fechter, T.; Doll, C.; Volegova-Neher, N.; Henne, K.; Scholber, J.; Knippen, S.; Kirste, S.; Grosu, A. L.; and Jilg, C. A. 2013. 3 Tesla multiparametric MRI for GTV-definition of Dominant Intraprostatic Lesions in patients with Prostate Cancer—an interobserver variability study. *Radiation oncology (London, England)*, 8: 183–183.
- Rodieck, R. 1965. Quantitative analysis of cat retinal ganglion cell response to visual stimuli. *Vision Research*, 5(12): 583–601.

Ronneberger, O.; Fischer, P.; and Brox, T. 2015. U-Net: Convolutional Networks for Biomedical Image Segmentation. *Medical Image Computing and Computer-Assisted Intervention – MICCAI 2015*, 234–241.

Simpson, A. L.; Antonelli, M.; Bakas, S.; Bilello, M.; Farahani, K.; van Ginneken, B.; Kopp-Schneider, A.; Landman, B. A.; Litjens, G.; Menze, B. H.; Ronneberger, O.; Summers, R. M.; Bilic, P.; Christ, P. F.; Do, R. K. G.; Gollub, M.; Golia-Pernicka, J.; Heckers, S.; Jarnagin, W. R.; McHugo, M.; Napel, S.; Vorontsov, E.; Maier-Hein, L.; and Cardoso, M. J. 2019. A large annotated medical image dataset for the development and evaluation of segmentation algorithms. *arXiv preprint arXiv:1902.09063*.

Singh, S. P.; Wang, L.; Gupta, S.; Goli, H.; Padmanabhan, P.; and Gulyás, B. 2020. 3D Deep Learning on Medical Images: A Review. *Sensors*, 20(18).

Spohn, S. K.; Bettermann, A. S.; Bamberg, F.; Benndorf, M.; Mix, M.; Nicolay, N. H.; Fechter, T.; Hölscher, T.; Grosu, R.; Chiti, A.; Grosu, A. L.; and Zamboglou, C. 2021. Radiomics in prostate cancer imaging for a personalized treatment approach - current aspects of methodology and a systematic review on validated studies. *Theranostics*, 11: 8027–8042.

Steenbergen, P.; Haustermans, K.; Lerut, E.; Oyen, R.; De Wever, L.; Van den Bergh, L.; Kerkmeijer, L. G.; Pameijer, F. A.; Veldhuis, W. B.; van der Voort van Zyp, J. R.; Pos, F. J.; Heijmink, S. W.; Kalisvaart, R.; Teertstra, H. J.; Dinh, C. V.; Ghobadi, G.; and van der Heide, U. A. 2015. Prostate tumor delineation using multiparametric magnetic resonance imaging: Inter-observer variability and pathology validation. *Radiotherapy and Oncology*, 115(2): 186–190.

Sudre, C. H.; Li, W.; Vercauteren, T. K. M.; Ourselin, S.; and Cardoso, M. J. 2017. Generalised Dice overlap as a deep learning loss function for highly unbalanced segmentations. *Deep learning in medical image analysis and multimodal learning for clinical decision support*, 240–248.

Taha, A. A.; and Hanbury, A. 2015. Metrics for evaluating 3D medical image segmentation: analysis, selection, and tool. *BMC Medical Imaging*, 15(1): 29.

Tian, Z.; Li, X.; Zheng, Y.; Chen, Z.; Shi, Z.; Liu, L.; and Fei, B. 2020. Graph-convolutional-network-based interactive prostate segmentation in MR images. *Medical Physics*, 47(9): 4164–4176.